Photoinduced Electron Transfer Between Pyridine Coated Cadmium Selenide Quantum Dots and Single Sheet Graphene

Shirui Guo, Duoduo Bao, Srigokul Upadhyayula, Wei Wang, Ali B. Guvenc, Jennifer R. Kyle, Hamed Hosseinibay, Krassimir N. Bozhilov, Valentine I. Vullev, Cengiz S. Ozkan,* and Mihrimah Ozkan**

Interest in graphene as a two-dimensional quantum-well material for energy applications and nanoelectronics has increased exponentially in the last few years. The recent advances in large-area single-sheet fabrication of pristine graphene have opened unexplored avenues for expanding from nano- to meso-scale applications. The relatively low level of absorptivity and the short lifetimes of excitons of single-sheet graphene suggest that it needs to be coupled with light sensitizers in order to explore its feasibility for photonic applications, such as solar-energy conversion. Red-emitting CdSe quantum dots are employed for photosensitizing single-sheet graphene with areas of several square centimeters. Pyridine coating of the quantum dots not only enhances their adhesion to the graphene surface, but also provides good electronic coupling between the CdSe and the two-dimensional carbon allotrope. Illumination of the quantum dots led to injection of n-carrier in the graphene phase. Time-resolved spectroscopy reveals three modes of photoinduced electron transfer between the quantum dots and the graphene occurring in the femtosecond and picosecond time-domains. Transient absorption spectra provide evidence for photoinduced hole-shift from the CdSe to the pyridine ligands, thereby polarizing the surface of the quantum dots. That is, photoinduced electrical polarization, which favors the simultaneous electron transfer from the CdSe to the graphene phase. These mechanistic insights into the photoinduced interfacial charge transfer have a promising potential to serve as guidelines for the design and development of composites of graphene and inorganic nanomaterials for solar-energy conversion applications.

1. Introduction

Recent advances in photovoltaics have demonstrated that composites of graphene and quantum dots (QDs) are promising candidates for energy-conversion applications.[1] The ability to attain graphene sheets with relatively large areas, along with its metallic-like lateral electrical conductivity, has drawn the ever-growing interest on this carbon allotrope as the media of choice for collection and transport of photo-generated charge carriers in photovoltaic (PV) devices.[1e,2]

The absorbance of single-sheet graphene, however, does not exceed $\approx 10^{-2}$ in the visible region of the spectrum.[3] Furthermore, photoexcited graphene undergoes ultrafast relaxation to low-lying excited states (i.e., only tenths of eV above the ground state), with lifetimes of the optical phonons that barely exceed 1 ps.[4] These short lifetimes of graphene excited states, along with its relatively small absorptivity throughout the visible spectral region, present a principal shortcoming for the use of this carbon allotrope as a single sheet by itself for light-energy conversion applications.

Dr. S. Guo, Dr. A. B. Guvenc, Dr. J. R. Kyle, Prof. M. Ozkan
Department of Electrical Engineering
Department of Chemistry
University of California
Riverside, CA 92521 USA
E-mail: mihri@ee.ucr.edu

W. Wang, H. Hosseinibay, Prof. C. S. Ozkan
Materials Science and Engineering Program
Department of Mechanical Engineering
University of California
Riverside, CA 92521 USA
E-mail: cozkan@engr.ucr.edu

Dr. D. Bao, S. Upadhyayula, Prof. V. I. Vullev
Department of Bioengineering
Department of Chemistry
Department of Biochemistry
Center for Bioengineering Research
Materials Science and Engineering Program
University of California
Riverside, CA 92521, USA
E-mail: vullev@ucr.edu

Dr. K. N. Bozhilov
Department of Earth Sciences and Central Facility for Advanced Microscopy and Microanalysis
University of California
Riverside, CA 92521, USA

DOI: 10.1002/adfm.201203652

In graphene-based composites, often chalcogenide QDs are the principal light sensitizers because of their: (1) relatively long excited-state lifetimes; and (2) relatively large bandgaps, tunable between ≈1.5 and >3 eV. In the design of PV devices, bulk-heterojunction (BHJ)[1a] and tandem[1e] architectures allow not only for an increase in the contact area between the graphene phase and the QD sensitizers, but also for an increase in the overall light absorptivity of the composite films.

Zero-dimensional semiconductor nanoarchitectures, such as quantum dots, with their size-tunable optical and electronic properties, provide the means for attaining widely diverse hybrid structures with solid conductors or semiconductors.[5] The QD unique properties, such as relatively high energy conversion efficiency (beyond the Schockley–Queisser limit),[6] photostability, and size-controllable band gaps and redox properties, make them highly desirable for light harvesting applications.[7]

Implementing elegant multiscale architectures in quantum-dot-sensitized PV devices has allowed for concurrent attainment of increased light absorptivity, decreased paths of exciton migration (prior to charge separation), and efficient collection of charge carriers.[8] Conversely, BHJ materials provide facile means for constructing large-area PV devices that, while lacking the potential for high conversion efficiency, do not have the fabrication complexity of QD-containing structures requiring multiscale order.[9] In such heterophasic PV devices, one-dimensional conducting materials, i.e., quantum wires (QRs), provide pathways for long-range charge transport uninterrupted by interfaces, which is essential for increased carrier-collection efficiencies. Indeed, carbon nanotubes and other QRs have become intricate components of recently developed PV devices.[9b–d]

Alternatively, two-dimensional materials, such as quantum wells (QWs), provide unique capabilities for efficient collection of photogenerated charge carriers within the same phase, spread over large working areas.[1a,e,2b] The two-dimensional QW morphology of graphene, along with its high electron and hole mobility,[10] has made this carbon allotrope a desirable scaffold for optoelectronic and photovoltaic applications.[11]

Many of the proposed QD/QW hybrid material for PV applications employ graphene oxide (GO) or reduced graphene oxide (RGO) as QW.[1a–c,12] The dispersion of graphitic carbon into exfoliated sheets of GO offers chemical-based approaches for producing RGO sheets.[2d,12b] Reduction of GO sheets, however, allows only for a partial restoration of the sp^2 network.[13]

As an alternative, others and we have employed chemical vapor deposition (CVD) for growing films of graphene with structural and electronic properties superior to those of RGO.[14] Most importantly, size scalability of graphene films grown via CVD is the key advantage for meeting the requirements for fabricating large-area PV and other optoelectronic devices: e.g., CVD allows for fabricating single-sheet graphene with areas exceeding five square inches.[14a,15]

Graphene is known to quench photoluminescence (PL) of cadmium chalcogenide QDs.[16] Three phenomena can account for the reported emission quenching: (1) resonance energy transfer; (2) electron-exchange energy transfer; and (3) charge separation. Non-radiative dipole-dipole resonance energy transfer (i.e., via Förster mechanism) does not require electronic coupling between the materials and can be effective between the QDs and the graphene surfaces even at distances that exceed 10 nm.[17] For high-symmetry systems, however, that involve transition quadrupoles and transition octapoles (instead of transition dipoles), the distances for efficient resonance energy transfer are shortened.[18]

Alternatively, electron-exchange energy transfer (i.e., via Dexter mechanism)[18] involves simultaneous oppositely directed electron-transfer processes: i.e., from the conduction band of the photoexcited QDs to the graphene and from the graphene to the valence band of the excited QDs. Because electron-exchange energy transfer requires electronic coupling between materials, its efficiency falls off considerably for interfacial QD-graphene distances exceeding about 1 nm. Furthermore, for such Dexter-type energy transfer, the rates of the two opposing electron transfer steps should be compatible. When one of the opposing electron-transfer processes is faster than the other, however, the QD-exciton deactivation results in charge separation: i.e., either electron or hole transfer from the QDs to the graphene. This photoinduced charge separation is the key process for light harvesting QD/QW materials, i.e., for converting absorbed light energy into free n- and p-carriers.

The balance between the three mechanisms of PL quenching in QD/graphene hybrids depends not only on the match between the electronic properties of the QDs and the graphene, but also on the media that separates the QD and the graphene. For example, coating with alkyl derivatives increases the stability and solubility of QDs. Such alkyl coatings, however, efficiently suppress charge transfer,[19] making resonance energy transfer to graphene the prevailing quenching pathway, as recently demonstrated for CdSe/ZnS QDs functionalized with trioctylphosphine oxide.[16a] Alternatively, when bare CdSe/ZnS QDs were deposited on graphene, their PL quenching resulted from photoinduced charge separation.[16b] Analogously to QD/QW, for QD/QR devices (i.e., devices of QDs on single-wall carbon nanotubes) stabilizing the CdSe QDs with coatings of small aromatic amines, i.e., pyridine, was essential for attaining photoconversion.[20]

Herein, we utilized large-area CVD-fabricated single-sheet graphene to investigate the interfacial photoinduced charge transfer between pyridine-coated CdSe QDs and the carbon allotrope. Although the Fermi level of graphene lies between the valence and the conduction band of the inorganic particles, we observed preferential directionality of the photoinduced electron transfer from CdSe phase to the carbon allotrope.

Time-resolved spectroscopy revealed three modes of photoinduced charge separation: (1) a picosecond transfer of relaxed electrons from CdSe to graphene; (2) a sub-picosecond transfer high-energy carriers to graphene; and (3) a direct excitation to CdSe-graphene charge-transfer states. In addition, we observed evidence for pico- and subpico-second formation of pyridine radical cation, indicating hole transfer from the CdSe phase to the aromatic coating ligands. Concurrently, the photoelectric properties of the QD/QW films revealed that the light-induced processes populated the graphene phase with n-carriers, indicating for photoinduced transfer of electrons from the CdSe to the carbon allotrope. While the hole shift to the coating pyridine ligands would decrease the overall distance for electron transfer from the graphene phase, this process was less favorable than the electron transfer from the chalcogenide to the carbon

allotrope. We ascribed the observed preferred directionality of photoinduced electron transfer from the QDs to the relatively large reorganization energy for injecting holes at energy levels considerably below the graphene Dirac points.

2. Results and Discussion

2.1. Hybrid Films of Quantum Dots and Graphene

A method based on CVD allowed us to synthesize single layers of graphene with areas of about 10 cm^2, as we have previously reported.[14d] We deposited the graphene on smooth substrates such as glass and silicon, and characterized it using Raman spectroscopy and fluorescence quenching microscopy.[14e]

For a light-sensitizer of the hybrid films, we employed CdSe QDs that were coated with octadecylamine (ODA) or pyridine (Py). We used commercially available ODA-coated QD samples that were a 3:2 mixture (**Figure 1**) of CdSe and ZnS crystals with an average diameter of about five nanometers as determined by transmission electron microscopy (TEM). Because of the bandgap difference between the two materials, we could selectively photoexcite the CdSe QDs in the visible and near UV regions without interference from the ZnS particles. Therefore, we can regard the light-absorbing material as predominantly CdSe QD photosensitizers diluted with ZnS QDs, and hence our discussion focuses on the former. Treating of QD-ODA with Py resulted in an exchange of the aliphatic with the aromatic ligands as we confirmed using infrared spectroscopy. As determined with TEM, the treatment with pyridine did not alter the inorganic components of the particles (Figure 1b).

Covalent grafting of graphene with functional materials requires breaking of its π-conjugation. Therefore, we resorted to non-covalent self-assembly to coat the graphene surfaces with QDs. Dropping diluted suspensions of pyridine-coated QDs on the surfaces of the carbon allotrope, followed by multiple washes, produced hybrid graphene films with organically coated inorganic nanoparticles. We observed that pyridine coatings of the QDs was essential for obtaining densely packed monolayers of QDs with minimum clumps over large areas of graphene (Figure 1c,d). The QD-Py nanoparticles tend to form monolayer islands with density of about 1.14 particles per 100 nm^2 calculated from SEM images (Figure 1d). The ODA-coated QDs did not manifest the same propensity for self-assembly in monolayers on the carbon substrate (Supporting Information Figure S1). Hence, the balance between the interfacial energies between the three phases, i.e., the solvent (pyridine/toluene), the graphene and the pyridine coatings, provided

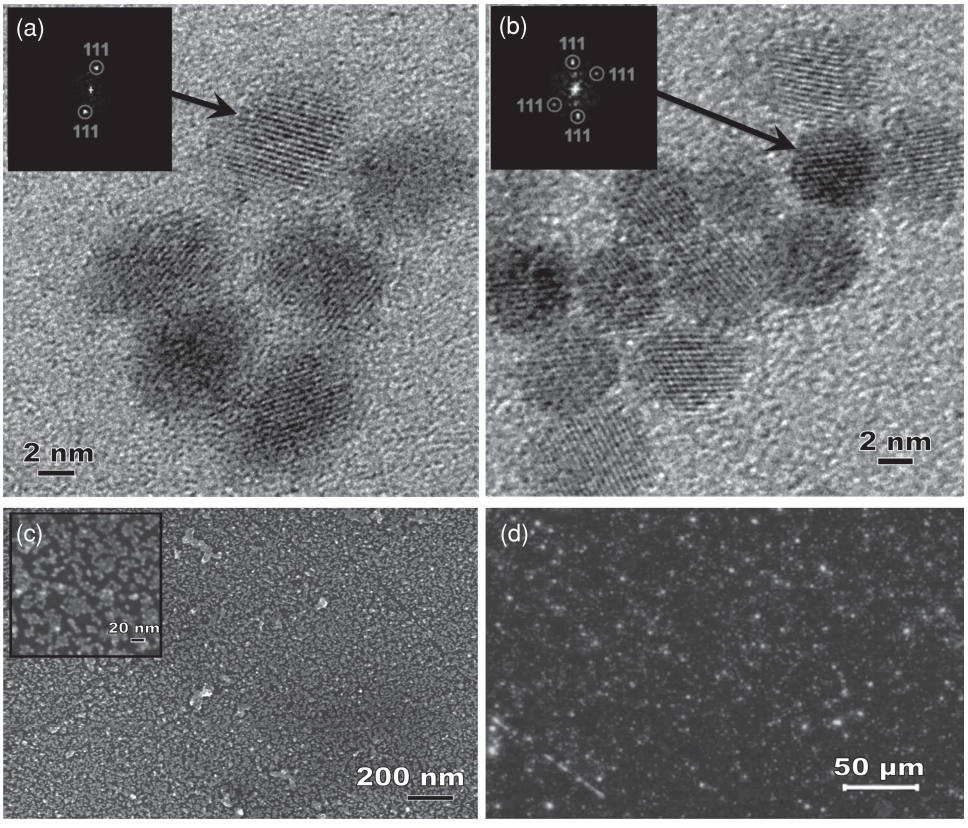

Figure 1. Microscopy images of quantum dots (QDs) and of QD films. a,b) Representative transmission electron microscopy (TEM) images of a) QD-ODA, and b) QD-Py. Insets: FFTs of the lattice images of selected particles. The reflections were estimated to be from {111} planes of cubic CdSe, as indexed in the FFTs of the lattices. c) Scanning electron microscopy (SEM) image of QD-Py/graphene film. Inset: SEM image of the film at higher magnification. d) Confocal fluorescence microscopy image of QD-Py/graphene film (λ_{ex} = 488 nm with10-nm bandwidth; and λ_{em} = 624 nm with 40-nm bandwidth).

the optimal conditions for self-assembly of monolayers of QDs on single-sheet graphene. Liu et al. reported on aqueous processable composite of pyridine functionalized CdSe QDs and chemically converted graphene and described opportunities for graphene based photovoltaic devices.[21]

Coating of QDs with pyridine indeed enhances their adherence to carbon-based surfaces, such as highly oriented pyrolitic graphite and carbon nanotubes,[22] which was in agreement with our observations (Figure 1c,d). To drive the fomation of QD monolayers on graphene, the pyridine moieties had to provide an approach for sufficiently strong adhesion between the CdSe QDs and the carbon allotrope. With the coordination bond between pyridine and a metal ion, such as cadmium and zinc, lying on the plane of the aromatic ring, the organic ligands in the QD-Py would be oriented away from the surfaces of the inorganic nanoparticles.[23] Therefore, at the point of contact between a QD-Py and graphene, the pyridine aromatic rings are unlikely to orient in parallel to the surface of the carbon allotrope (without introducing significant bond tension). As a result, π–π stacking cannot account for the observed adhesion, as it has been previously suggested for adsorption of Py-coated nanoparticles to similar carbon allotropes.[2c,20,22a,22c] Considering the structural features of the face-to-edge interactions between aromatic residues in proteins and other biomolecules,[24] we ascribed the observed QD-Py adhesiveness to favorable contacts between the graphene π-conjugation and the edges of the obliquely oriented pyridine ligands.

2.2. Absorption and Emission Properties of the Hybrid Films

The exchange of the aliphatic ligands, ODA, with the aromatic amine, Py, caused only about three-to-four nanometer red shifts in the QD absorption and emission spectra, corresponding to about a 0.01 eV decrease in the optical band gap (**Figure 2**a). When deposited as films on glass surfaces, the pyridine-coated QDs exhibited about five-to-seven nanometer red shift and broadening of their spectral features (Figure 2b), which was consistent with electronic coupling between the QDs when clustered into the solid assemblies. Overall, the optical band gap of the CdSe QDs was about 2 eV, as estimated from the absorption and emission spectra analogously to estimating the zero-to-zero energy, E_{00}, of organic chromophores (Figure 2a,b).

Conversely, the presence of graphene had a pronounced effect on the pyridine-coated QDs (Figure 2b). The single-sheet graphene induced: (1) a loss of fine structure and broadening of the QD-Py absorption spectra (as apparent at the red edge); and (2) quenching of the QD emission (Figure 2b). The former was indicative of ground-state electronic coupling between the confined CdSe states and the graphene, i.e., coupling mediated through the pyridine layer separating the carbon substrate from the CdSe semiconductor (**Scheme 1**). The latter was indicative of efficient photoinduced processes that deactivated the CdSe excited states, i.e., processes such as charge or energy transfer occurring in time scales shorter than the lifetimes of the CdSe excited states that decay radiatively. Indeed, while the emission quantum yield, Φ, of the QD-Py films on glass was 0.028 ± 0.003, the values of Φ for the QD-Py mono-layer on graphene ranged between about 2×10^{-4}–2×10^{-3}.

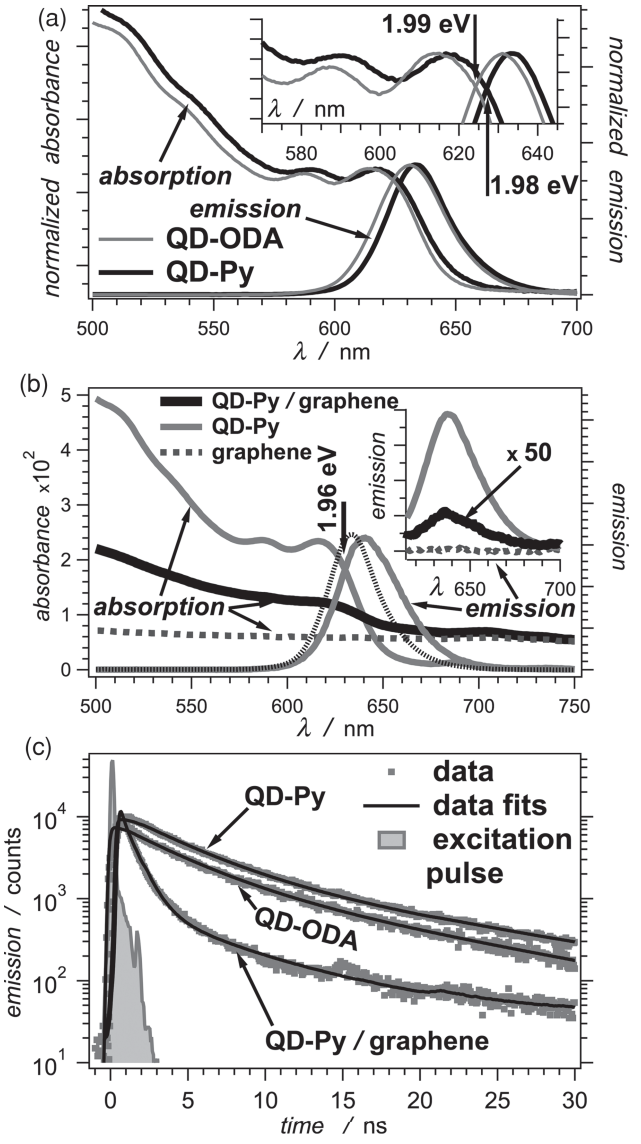

Figure 2. a) Comparison between the normalized steady-state absorption and emission spectra of QD-ODA and QD-Py suspended in toluene (λ_{ex} = 420 nm). b) Steady-state absorption and emission spectra of QD-Py films, single-layer graphene and QD-Py/graphene hybrid. The absorption spectra of the solid films were obtained from reflectance measurements using an integrating sphere, and the emission spectra were recorded using a small-angle setup (for the main panel, λ_{ex} = 420 nm; and for the inset, λ_{ex} = 600 nm). For improved visualization, the emission spectra of graphene and of QD-Py/graphene were scaled up by a factor of 50. The stripe-patterned black line corresponds to the solution QD-Py emission spectrum. c) Emission decays of QD-Py films, QD-ODA films and QD-Py/graphene hybrid, with the corresponding multiexponential data fits, plotted against logarithmic ordinate. The time-resolved emission data were recorded at 630 nm using TCSPC (λ_{ex} = 406 nm, excitation pulse width = 195 ps). For estimation of the QD band gaps, the zero-to-zero energy was calculated from the crossing points of the normalized steady-state absorption and emission spectra.

To quantify the observed graphene-induced quenching of the QD luminescence, we resorted to time-resolved emission spectroscopy, as implemented by time-correlated single-photon counting (TCSPC). Biexponential functions provided

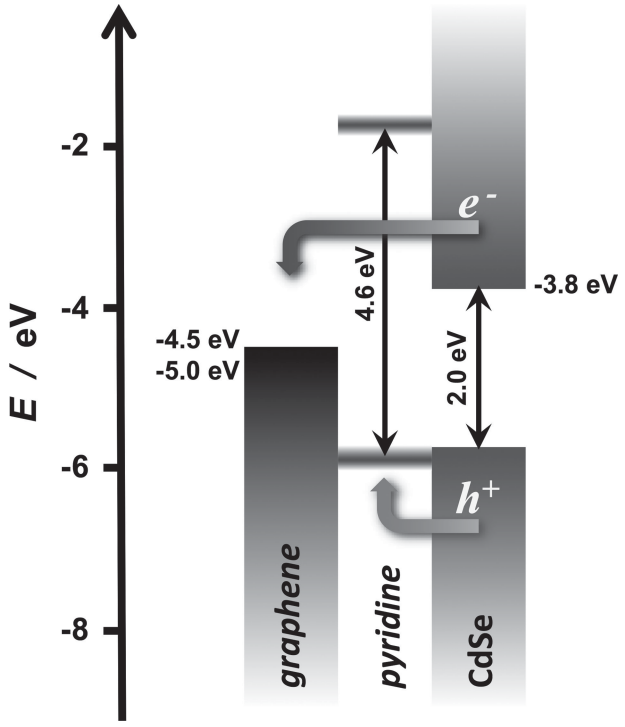

Scheme 1. Band diagram and charge transfer between pyridine-coated CdSe QDs and graphene.

reasonably good fits for the emission decays of the QDs deposited on glass with no graphene (Figure 2c).[19,25] The fits produced principal components with lifetimes ranging between 3 and 4 ns, and minor components with lifetimes longer than 10 ns (Figure 2c). Multiexponential functions fitting for QD-Py/graphene yielded average lifetimes smaller than about 0.5 ns (Figure 2c)

In the absence of graphene, the exchange of the organic ligands of the QDs had a negligible effect on the observed emission decays (Figure 2c): i.e., trend of slight decrease in the lifetimes upon exchanging ODA with Py was within the experimental uncertainty. When QD-Py nanoparticles were deposited on graphene, however, their emissive states exhibited predominantly short lifetimes, i.e., in the sub-nanosecond time domain (Figure 2c). This finding demonstrated that coating the QDs with small aromatic ligands not only drove their self-assembly into monolayers over the graphene, but also provided considerable electronic coupling between the semiconducting chalcogenide and the carbon allotrope essential for mediating photoinduced processes responsible for the observed emission quenching.

Comparison of the emission quantum yields, Φ, obtained from different QD-Py/graphene samples (from steady-state measurements) with their emission lifetimes, τ (from TCSPC), presented a discrepancy with important implications. While the measured emission-decay lifetimes from the different QD-Py/graphene samples exhibited only about two-fold variations between the samples, the corresponding values of Φ varied about an order of magnitude, i.e., they were between ≈15 and ≈150 times smaller than Φ of the QD-Py films on glass. In contrast, the values of τ of the QD-Py/graphene samples were only 10–20 times smaller than τ of QD-Py films deposited on bare glass without graphene.

We ascribe this discrepancy to the inherent heterogeneity of the solid-film samples. While most of the QDs were deposited as monolayers on the graphene, multilayered clusters of QDs (i.e., film imperfections) were the principal source of the PL. The emission quantum yield averages the properties of all QDs deposited on the graphene. In the monolayers, all QDs were in direct contact with graphene. The multilayers, however, contained QDs that were not in contact with graphene. Should Φ of the multilayered QDs exceed with at least two orders of magnitude Φ of the monolayered QDs, a few percent variations in the amount of clustered QDs (from a sample to sample) would alter the measured ensemble-average emission quantum yield with an order of magnitude or more, which was consistent with our observations.

Fluorescence microscopy allowed us to confirm the origin of the observed discrepancy between the trends in the values of τ and Φ for the QD-Py/graphene samples. SEM images of QD-Py/graphene samples revealed relatively dense coverage of surfaces with nanoparticles, (Figure 1c). Confocal fluorescence microscopy images of the same films showed that most of the areas covered with the QD-Py nanoparticles were dark (Figure 1d). Concurrently, the same images of the QD-Py/graphene films also showed spots with high emission intensity, which we attributed to agglomerated sites of pyridine-coated QDs on the graphene film (Figure 1d), i.e., sites containing QDs that lack sufficient electronic coupling with the graphene.

These results suggested that the QD-Py/graphene PL from the strongly luminescent QD clusters dominated the emission from the spectroscopy measurements (Figure 2b). If the mono-layered pyridine-coated QDs were not luminescent (i.e., if the τ values of the graphene-quenched PL of the QD-Py nanoparticles did not exceed a few picosecond, which is under the dynamic range of TCSPC), variations in the amount of multilayered QDs would change the PL intensity (and hence the calculated Φ), but would not alter to the same extent the rates with which these clustered QDs decay radiatively. Thus, the emission quenching rate constant of about 5×10^9 s^{-1}, extracted from TCSPC measurements, represented the photoinduced process mostly from the clustered QDs that were not in a direct contact with the graphene surface.

2.3. Transient-Absorption Dynamics

To overcome the limitation of emission spectroscopy and to discover the real interaction between monolayer QDs and graphene, we employed pump-probe transient-absorption spectroscopy that allowed us to monitor transitions involving the confined CdSe states regardless of their radiative characteristics.[25] Transient absorption (TA) spectra of the QD films on glass exhibited the characteristic features of transitions between confined states of cadmium chalcogenide nanocrystals (**Figure 3**).[26] Within the first few hundred femtoseconds after the excitation, the Stark effect from the photoinduced redistribution of charge carriers manifested itself in: (1) bleaching of the ground-state absorption resulting in B_i bands; and (2) shifts in the energy levels of

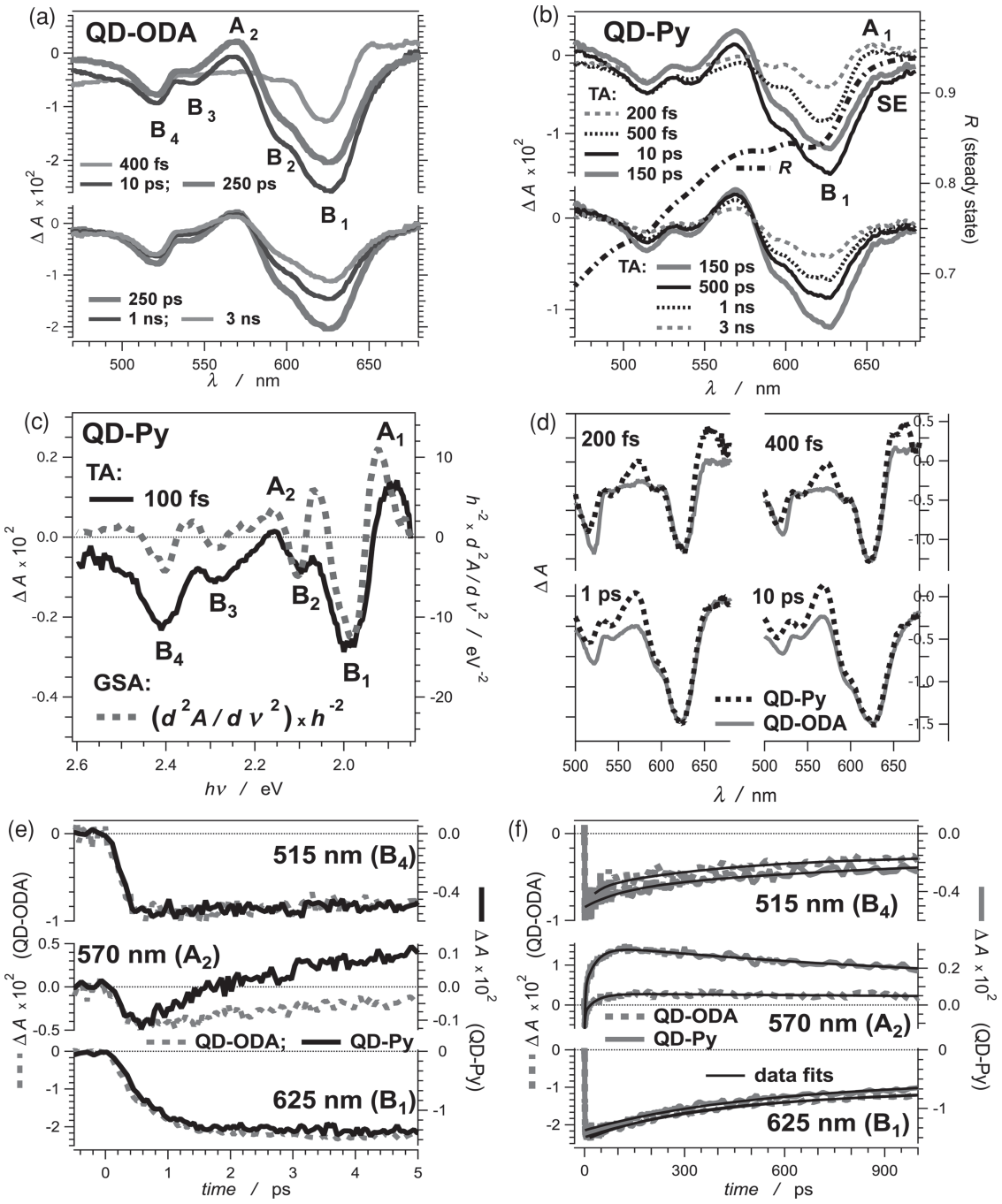

Figure 3. Transient absorption (TA) dynamics of QD films deposited on glass with no graphene. a) TA spectra of a QD-ODA film recorded at different times after the excitation. (b) TA spectra of a QD-Py film in comparison with its reflectance, *R*, from which the ground-state absorbance was determined ($A_{400\,nm} = 0.10$). The weak negative signal at ≈650 nm ws ascribed to the stimulated emission (SE). c) Comparison between an early-time TA features and the second derivative of the ground-state absorption (GSA) of a QD-Py film, with the corresponding assignments of the absorption, A_i, and bleaching, B_i, bands. d) Comparison between B_1-normalized TA spectra of QD-ODA and QD-Py films. e,f) TA kinetic curves of QD films recorded at three spectral regions. For ease of comparison, the curves were plotted against different ΔA ordinates, normalizing the initial bleach minima. At 625 nm, biexponential data fits of the bleach recovery yielded: for QD-ODA $\tau_1 = 250 \pm 20$ ps ($\alpha_1 = -0.45$), $\tau_2 = 1.9 \pm 0.7$ ns ($\alpha_2 = -0.32$), and an offset $\alpha_\infty = -0.22$; for QD-Py $\tau_1 = 260 \pm 50$ ps ($\alpha_1 = -0.34$), $\tau_2 = 1.6 \pm 0.6$ ns ($\alpha_2 = -0.43$), and an offset $\alpha_\infty = -0.23$. ($\lambda_{pump} = 400$ nm, 1.5 μJ per pulse, 38-fs pulse width of the fundamental at 800 nm.)

the states associated with the optical transitions, resulting in A_i bands at the blue or red edges of the B_i bands (Figure 3a–c).[26a] The similarity between the early-time TA spectra and the second derivative of the ground-state absorption of the CdSe QDs was in accord with the Coulombic origin of the A_i and B_i features that appeared immediately after the excitation (Figure 3c).[27]

The further growth of the B_1 and B_2 bands, which continued for a few picoseconds after the excitation pulse, was ascribed

to the dynamics of intraband relaxation.[26a] Indeed, sub-picosecond and picosecond intraband relaxation of the photoexcited CdSe QDs, leading to filling of the low-lying $1S_e$ quantum size level (QSL) with electrons,[28] further enhances the magnitude of the B_1 and B_2 TA bands.[26a] At the high-energy transitions (e.g., at 530–515 nm) within about 400 fs, ΔA reached its most negative values (Figure 3e). In comparison, the B_1 and B_2 bands manifested slower growth, exhibiting multiexponential kinetics with $\tau \approx 1$ ps, to reach their most negative ΔA values at about 5 ps (Figure 3e). This picosecond growth of B_1 and B_2 was consistent with the filling of the low-lying QSLs in the conduction band (CB) with electrons via intraband relaxation.[26a]

The recovery of the ground state absorption (i.e., the bleach recovery) manifested biexponential kinetics, which was quite similar for the QD-ODA and QD-Py films with no graphene (Figure 3f). For the QD-ODA and for QD-Py, the time constants, τ, of the fast components of the bleach recovery at the B_1 bands were about 250 ps, and of the slow components–close to 2 ns (Figure 3f). The nanosecond slow-components of the TA kinetics, however, should be viewed with caution in a somewhat qualitative manner. The upper limit of the time dynamic range of the pump-probe setup was 3.2 ns. Therefore, we cannot claim statistical significance for values of τ exceeding ≈1 ns: i.e., it is challenging to claim statistical discernibility between such time constants that are relatively long for the recorded datasets, and the baseline offset, $\alpha_\infty \approx \alpha_{\text{unrecoverable TA}} + \Sigma\alpha_i \exp(-t/(\tau_i >> 1\text{ ns}))$. Meanwhile, fitting the B_1 kinetics with triexponential functions, in which we introduced the lifetime values from the TCSPC studies (Figure 2) and kept them fixed, yielded similar time constants, τ_1, for the fast components. This latter triexponential analysis, however, required an assumption that the kinetics of the bleach recovery at 625 nm followed the kinetics of deactivation of the PL states of the CdSe.

Do pyridine ligands affect the excited-state kinetics of the QDs? The TA spectra of the QD-ODA and the QD-Py films had quite similar TA features. In the B_1 and B_2 spectral regions, they exhibited practically the same TA kinetics (Figure 3a,b,e,f). Conversely, a closer examination of the TA spectra at the region between 520 and 570 nm reveled that QD-Py films had consistently more positive ΔA than QD-ODA films, which persisted over tens of picoseconds (Figure 3d). The TA kinetic curves recorded at 570 nm further illustrate this trend (Figure 3e,f). Such TA feature has been previously reported for pyridine-coated CdSe QDs and was ascribed to the radical-cation transient of the ligand ($Py^{+\bullet}$).[29] Indeed, pyridine is a hole scavenger for chalcogenide QDs.[30] The absorption of the $Py^{+\bullet}$ transient extends from the near UV to the mid visible spectral region,[31] and in the TA spectra of pyridine-coated CdSe QDs, it appears as a weak broad band at wavelengths shorter than ≈570 nm.[29] Our findings, therefore, suggested that QD-Py films exhibited a charge-transfer excited state, in which the holes resided on the pyridine ligands.

Deposition of pyridine-coated QDs on single-sheet graphene dramatically changed their TA dynamics (**Figure 4**). The bleach recovery at the B_1 band had two principal components with time constants of about 20 and 300 ps (Figure 4b), which was consistent with previously reported rates of photoinduced electron transfer between CdSe QDs and single-wall carbon nanotubes.[32]

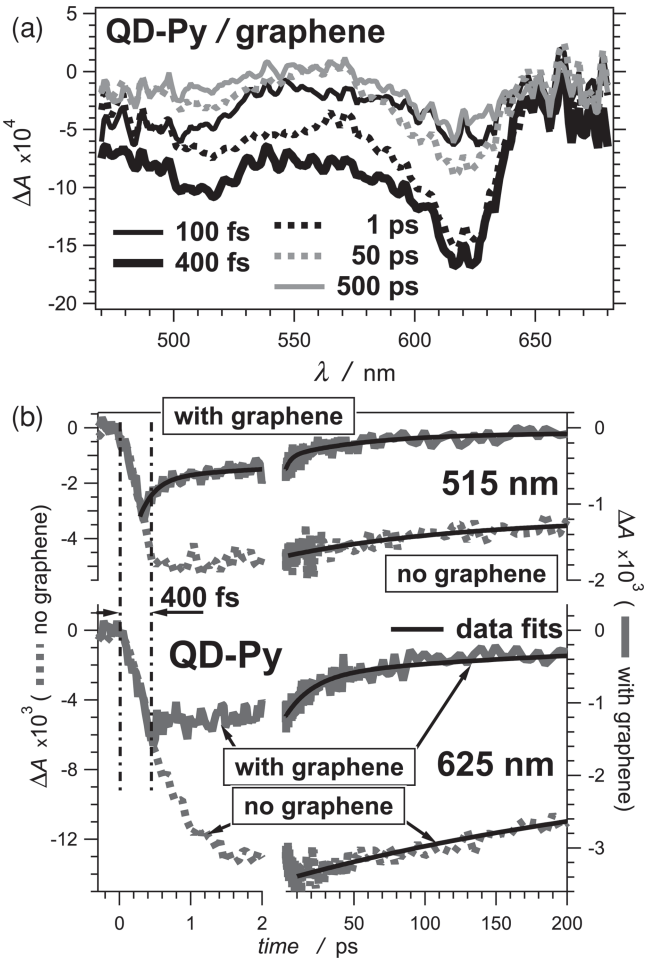

Figure 4. Transient absorption (TA) dynamics of QD-Py films deposited on single-sheet graphene on glass substrates. a) TA spectra of monolayers of pyridine-coated QDs deposited on graphene recorded at different times after the excitation. For improved signal-to-noise ratios, the samples were composed of stacks of three cover slips, with single-side deposited QD-Py/graphene monolayers (ground-state sample absorption at the excitation wavelength: $A_{400\text{ nm}} = 0.11$). b) Comparison between the kinetics, recorded at the B_1 and B_4 bands, of pyridine-coated QDs deposited on graphene and on bare glass. For visualization of the sub-picosecond dynamics, the early time-scale (i.e., for $t \leq 2$ ps) was extended. For the graphene samples multiexponential data fits of the bleach recovery yielded: at 625 nm, $\tau_1 = 19 \pm 3$ ps ($\alpha_1 = -0.49$), $\tau_2 = 270 \pm 50$ ps ($\alpha_2 = -0.42$), and an offset $\alpha_\infty = -0.09$; and at 515 nm, $\tau_1 = 260 \pm 60$ fs ($\alpha_1 = -0.44$), $\tau_2 = 3.9 \pm 1.2$ ps ($\alpha_2 = -0.23$), $\tau_3 = 60 \pm 11$ ps ($\alpha_3 = -0.27$), and $\alpha_\infty = -0.06$ ($\lambda_{\text{pump}} = 400$ nm, 1.5 μJ per pulse, 38-fs pulse width of the fundamental at 800 nm.)

The TA kinetic curves for QD-Py/graphene, however, did not exhibit the picosecond features of intraband relaxation that we observed for the other QD films. For the samples without graphene the growth of the B_1 band continued a few picoseconds after the excitation (Figure 3e, 4b). For QD-Py/graphene films, ΔA at 625 nm grew to its minimum within about 400 fs, prior to initiating the bleach recovery (Figure 4b). Similarly, the bleach recovery at 515 nm for QD-Py/graphene samples exhibited considerably faster rates than the rates of the B_4 dynamics of the other QD samples (Figure 4b). For QD-Py/graphene, ΔA

at 515 nm reached its minimum at about 300 fs, followed by bleach recovery with a sub-picosecond principal kinetic component: τ_1 = 0.26 ps with α_1 =–0.44 (Figure 4b). Because the B bands are indicative of populating the low-lying QSLs in the conduction band with electrons,[26a] these kinetic findings for QD-Py/graphene indicated that the photogenerated negative charge carriers were removed from the conduction band of CdSe prior to their picosecond intraband relaxation. Namely, some of the pathways of deactivation of the confined CdSe excited states involved unrelaxed charge carriers, such as "hot" electrons.[33]

A close examination of the TA spectra of the QD-Py/graphene films revealed the lack of the "dip" at 540–550 nm characteristic for the B_3 band, which was especially apparent for the sub-picosecond QD-Py spectra (Figure 4a cf. Figure 3b). While the negative ΔA values were indicative for the CdSe bleach bands in the QD-Py/graphene films, the broad TA spectral feature, between about 530 and 560 nm with slightly more positive ΔA, could be ascribed to the transients of oxidized pyridine, $Py^{+\bullet}$. The low absorptivity of the $Py^{+\bullet}$ transient in comparison with the CdSe TA B_i bands, along with the inherently small signal-to-noise ratio of the TA of monolayered QD-Py/graphene films, makes this interpretation somewhat challenging. The formation of $Py^{+\bullet}$ upon photoexcitation of pyridine-coated CdSe QDs, however, was consistent not only with the comparison between the QD-Py and QD-ODA films without graphene (Figure 3d), but also with previous reports on similar nanoparticles.[29]

Another characteristic of the TA for the QD-Py/graphene was the noticeably small ΔA values. The ground-state optical density at the excitation wavelength was similar for all samples within a factor of two. Concurrently, the ΔA values for the TA of QD-Py/graphene films were consistently about an order of magnitude smaller than the ΔA values of the QD-Py films without graphene (Figure 3 and Figure 4). This finding indicated that a part of the absorbed light energy did not generate excited states with TA features in the visible region of the spectrum. A plausible explanation could be sought in the direct photoexcitation to charge-transfer states between the CdSe and the graphene phase. (Indeed, such relatively long-range interfacial charge separation does not have TA features detectible in the visible region of the spectrum, consistent with the electron-transfer induced TA bleach recovery.[32,34]) As we mentioned above, the broadening of the QD-Py/graphene ground-state absorption in comparison with the QD films with no graphene (Figure 2b), suggested for a relatively strong electronic coupling between the CdSe and the graphene that would be essential for a direct photoexcitation to states with such long-range charge-transfer character.

Control sample of ODA-coated QDs on graphene showed smaller effect on the TA dynamics (Supporting Information Figure S2). Most of the bleach recovery of B_1 for QD-ODA/graphene followed a biexponential pattern with time constants of about 0.2 and 2 ns. At early times, however, a fast positive change in the ΔA contributed to about 10% of the bleach recovery for the QD-ODA/graphene TA at 625 nm, i.e., τ_1 about 13 ps with α_1 = 0.13 (Figure 4b). Because this is a relatively small contribution to the TA kinetics we cannot readily ascribe it to the intrinsic properties of the QD-ODA/graphene films. While this fast TA feature is in agreement with the rates of charge transfer between CdSe QDs and carbon allotropes,[1,32] it can also be representative of a small population of QDs that have defects in their coatings at the interface with graphene: i.e., defects that provide pathways for pronouncedly efficient quenching of the states responsible for the B_1 band.

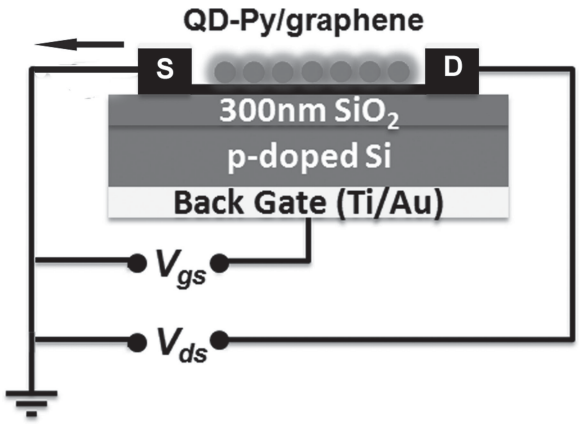

Scheme 2. Field effect transistor (FET) with hybrid film deposited on the insulating SiO_2 layer over the gate, and providing electrical contact between the source (S) and the drain (D).

2.4. Photoelectric Properties of the Hybrid Films

To examine if the observed PL quenching and the accelerated bleach recovery of the Py-coated QDs deposited on graphene were a result of photoinduced electron transfer from the CdSe to the carbon allotrope, we fabricated field effect transistor (FET) devices incorporating QD-Py/graphene hybrid films (**Scheme 2**). Using CVD, we patterned single-sheet graphene on p-doped silicon wafer covered with thin insulating layer of SiO_2. Gold strips formed source and drain contacts, and the graphene with the isolated Si substrate formed the gate (Scheme 2).

Due to this lack of continuous network (Figure 1d), the QD-Py layer did not provide a direct electrical contact between the source and the drain, as evident from the lack of detectible conductivity in the FET devices that did not contain graphene. Concurrently, the carrier mobility that we estimated for single-sheet graphene from the FET devices without QDs was 1500 $cm^2\ V^{-1}\ s^{-1}$, which was at the lower end of reported values for charge mobility in CVD-grown graphene of about 1000 to 6000 $cm^2\ V^{-1}\ s^{-1}$.[35] Since the charge mobility in the carbon allotrope was considerably higher than that of the broken QD network, we concluded that the single-sheet graphene (rather than the QD layer) was the principal carrier-transporting medium for the FET devices.

Upon illumination, the conductivity of the QD-Py/graphene hybrid films increased, as evident from the increase in the slope of the curves showing the effect of the applied drain-source voltage, V_{ds}, on the measured current, I_{ds} (**Figure 5**a). Namely, illumination of the QD-Py nanoparticles (that were the principal light absorber in the film) increased the number of charge carriers in the graphene phase (that provided the

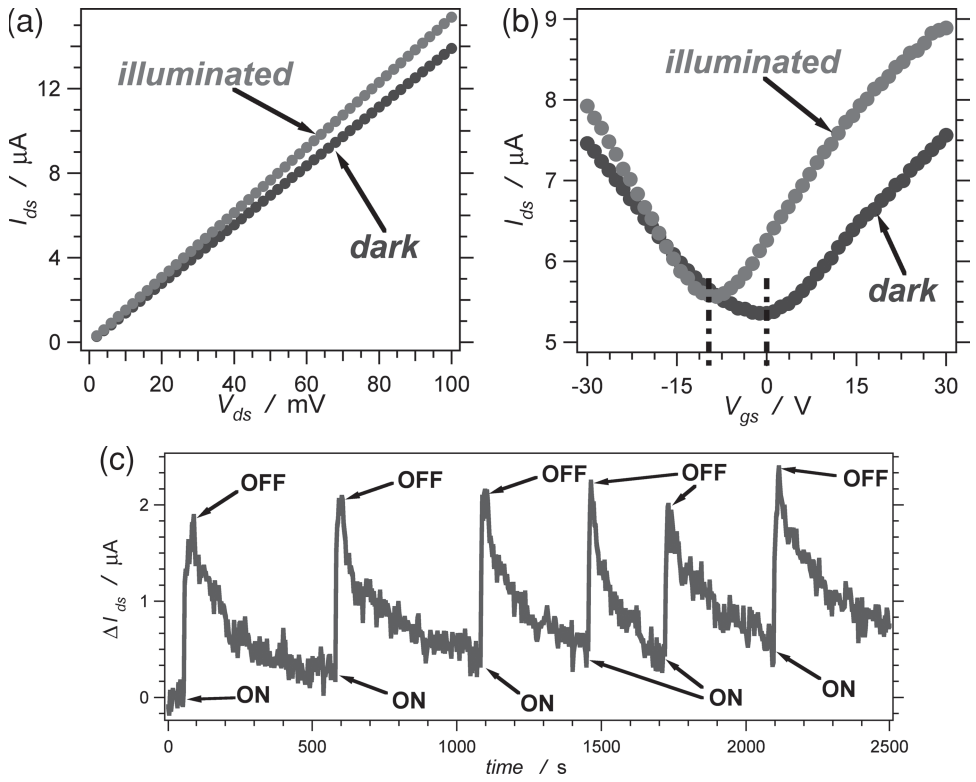

Figure 5. Current-voltage (*I–V*) characteristics of field-effect transistor FET devices comprising QD-Py/graphene films under illumination ($\lambda = 365$ nm, 0.2 W cm^{-2}) and under dark conditions. a) Representative drain-source current-voltage lines for a FET device with the illumination on and off (V_{gs} = 0 V). b) Representative *I–V* curves showing the dependence of the drain-source current, I_{ds}, on the gate voltage, V_{gs}, with the illumination on and off ($V_{ds} = 0.1$ V). c) Photoinduced changes in the drain-source current of a FET device ($V_{ds} = 0.1$ V; $V_{gs} = 0$ V). The illumination on/off cycle involved turning the light on for 30 s, and keeping it off for 4 to 8 minute. The time constant of the current increase upon turning the illumination on was 4.3 ± 1.6 s; and the time constant of current decrease upon turning the illumination off was 140 ± 30 s.

electrical contact between the drain and the source), which was consistent with photoinduced charge transfer (i.e., transfer of electrons and/or holes) from the QDs to the carbon allotrope. In addition, the observed linearity in the current dependence on the voltage demonstrated metallic characteristics of the single-sheet graphene film.

Concurrently, the curves representing the dependence of I_{ds} on the applied gate voltage, V_{gs}, revealed n-doping of the graphene upon photoexcitation of the QDs. The illumination caused a negative shift in the Dirac point, i.e., in the minimum of I_{ds} vs V_{gs} at constant V_{ds} (Figure 5b), which was indicative of n-doping of the conductive media.[36] Because the graphene, and not the QD layer, acted as a carrier channel in the FET devices, this light-induced n-doping of the conducting media was an indication of injection of electrons from the QDs into the carbon allotrope. A collection of positive charges in the QD layer, i.e., positive front gating that opposes the potential of the back gate, would also cause a negative shift in the $I_{ds}/V_{back\ gate}$ Dirac point.[37] Both phenomena that could lead to the observed negative shift were consistent with prevalent photoinduced electron transfer from the CdSe to the graphene phase.

The kinetics of photoswitching of the FET devices provided evidence for long-lived photoinduced charging of the QD-Py/graphene films (Figure 5c). Turning on the illumination of the QD films caused an increase in I_{ds}, which reached saturation within a few seconds, $\tau \approx 4$ s (Figure 5c). Although the rate constants of the photoinduced charge transfer exceeded 10^{10} s^{-1}, as estimated from the time-resolved spectroscopy studies, the kinetics of this I_{ds} jump represented the attainment of steady state between the light-driven influx of n-carrier into the graphene phase, the loss of the n-carriers via back charge transfer or trapping, and the in- and out-transport of the charge carriers through the source and drain terminals. Conversely, turning off the illumination did not cause a fast drop in I_{ds}. Instead, the measured current gradually decreased with a time constant of about 140 ± 30 s (Figure 5c), which was in agreement with previous reports on photoswitching mediated by hybrid materials of pyridine-coated CdSe QDs and carbon nanotubes.[20] This finding indicated that minutes after ceasing the illumination, photogenerated charge carriers still lingered in the film that was consistent with the energy-storage capabilities of graphene hybrid materials.[38]

2.5. Photoinduced Charge Transfer Between CdSe QDs and Graphene

The reported work function of graphite is 4.5–5.0 eV,[39] placing its Fermi level between the valence and the conduction band of the CdSe QDs (Scheme 1).[16b] Therefore, the photoexcited QDs can act as electron donors and as electron acceptors. Concurrently, the QDs can also act as energy donors, transferring their

excitons into the graphene phase via a resonance (Förster-like) or an electron-exchange (Dexter) mechanism.[17,18] In fact, Brus et al. have reported efficient resonance energy transfer from CdSe QDs (λ_{em} = 655 nm) to single-sheet graphene with time constants of about 250 ps.[16a] We observed similar dynamics for the deactivation of the CdSe excited state in the QD-Py/graphene films as illustrated by the principal emission decay time constant, $\tau_1 = 180 \pm 30$ ps (Figure 2c), and the slow component of TA B_1 recovery, $\tau_2 = 270 \pm 50$ ps (Figure 4b). Despite the similarities between our kinetic findings and the previously reported energy-transfer dynamics, we do not have evidence to prove or disprove whether this emission and TA dynamics was a result of energy-transfer processes mediated in the QD-Py/graphene films. Nevertheless, the photoinduced n-doping of the graphene (Figure 5b) indicated that the Py-coated CdSe QDs were preferentially electron donors.

The considerable increase in the rates of the TA bleach induced by the carbon allotrope (Figure 4b) was consistent with electron transfer from the CdSe to the graphene phase since the B_i bands were associated with populating with electrons of the low-lying QSLs in the chalcogenide conduction band.[32,34] Concurrently, the evidence for transients of oxidized pyridine, $Py^{+\bullet}$, suggested for oppositely directed photoinduced electron transfer, i.e., from the ligands to the vacated QSLs in the CdSe valence band. The latter process would place holes on the aromatic moieties between the chalcogenide and the carbon allotrope, considerably shortening the paths of electron transfer from the graphene to the QD-Py. Nevertheless, the photoelectrical findings indicated that the photoinduced electron transfer from the CdSe QDs to the graphene was faster than the oppositely directed charge transduction.

As previously indicated, the reorganization energy of the graphene phase provides the kinetic control responsible for the observed directionality of the photoinduced electron transfer from the QDs to the graphene.[16b] Electrochemically we estimated that the lowest energy level of the conduction band of the QDs was about –3.8 eV from vacuum level, placing the valence band at about –5.8 eV. Therefore, the graphene Fermi level, which for the non-doped allotrope crosses its Dirac points, was about 0.8 to 1.3 eV above the valence band of the CdSe nanocrystals (or the highest occupied molecular orbital, HOMO, of the pyridine ligands). Electron transfer from graphene to the valence band of CdSe or to the HOMO of pyridine, thus, requires coupling with a large-momentum phonon for generating a hole significantly offset in energy from the Dirac points.[16b,40] Hence, the electron transfer from graphene to the vacated HOMOs of the pyridines or QSLs in the valence band of the photoexcited CdSe requires significantly more energy dissipation than electron transfer from the conduction band of the CdSe QDs to the graphene.[16b] This larger reorganization energy for the electron transfer to the photoexcited pyridine-coated CdSe makes the hole transfer from the QDs slower than the electron transfer from the QDs to the graphene, which was consistent with our observations of preferential photoinduced n-doping of the conducting media of the QD-Py/graphene films.

As previously discussed, the TA findings suggested three modes of photoinduced electron transfer from the pyridine-coated QDs to graphene: (1) a twenty-picosecond transfer of "relaxed" electrons from the lowest QSLs of the CdSe conduction band; (2) a sub-picosecond transfer of "hot" electrons, prior to their interband relaxation; and (3) a direct photoexcitation to CdSe-graphene charge-transfer states. Meanwhile, the hole shift from the CdSe to the pyridine ligands (Figure 3d)[29] did not overcome the electron transfer from the QDs to the graphene. While reorganization energy would impede the hole transfer to the graphene phase, the accumulation of the holes in the pyridine ligands would polarize the surface of the QDs, i.e., generating electrets with the positive poles of their dipoles pointing to the exterior of the CdSe particles. Such polarization of the QD surfaces is still favorable for electron transfer from the CdSe phase.

3. Conclusions

Probing the electronic transitions between quantized levels in CdSe QDs provided evidence for three modes of interfacial photoinduced electron transfer from the inorganic chalcogenide to the graphene phase. The concurrent hole transfer from the CdSe to the pyridine ligands did not provide light-induce p-doping of the graphene, indicating that positive charges remained in the organic coatings of the QDs. Analogous to proton-coupled electron transfer,[41] the simultaneously occurring hole shift and electron transfer may prove importance for efficient interfacial charge transduction between semiconducting and organic media, which further paves way to discover new materials for photovoltaic devices.

4. Experimental Section

Materials Synthesis and Characterization: Graphene was synthesized using a copper foil as catalyst. Typically, the copper foil was cleaned with organic solvents and etched with acetic acid at 35 °C for 10 min to remove any surface oxides and other impurities. After washing it thoroughly, the copper was thermally annealed for 30 min by heating to 1000 °C in a reducing atmosphere: Ar/H_2 (flow rates 200:200 sccm, maintaining pressure of 2 Torr). While maintaining the same temperature, the annealed copper surface was exposed to methane for 20 min (at 100 sccm flow rate) mixed with H_2 at pressure elevated to 20 Torr. The metal sample, with the thus grown graphene on its surface, was cooled down to 25 °C at a cooling rate of 20 °C min^{-1}. The graphene-covered surface was coated with polymethylmethacrylate (PMMA) and the copper was etched with $FeCl_3$ (0.5 M aqueous solution). The PMMA-bound graphene sheet was washed thoroughly (with HCl (3%) and deionized water) and transferred to glass or to SiO_2-coated Si substrate. The PMMA layer was dissolved in organic solvent leaving the graphene sheet on the inorganic substrate.

Nanoparticles of CdSe, stabilized with octadecylamine, were purchased from NN-Labs, LLC (Fayetteville, AR). Although under the vendor's description, the particles (CZ620) were expected to have core/shell CdSe/ZnS architecture, TEM analysis revealed that the suspension contained mixture of about 58% CdSe nanocrystals (5.3 ± 0.4 nm), and 40% ZnS nanocrystals (5.2 ± 0.4 nm). About 80% of the CdSe nanocrystals were identified to have cubic sphalerite-type structure and the rest were hexagonal wurtzite-type. Most of the ZnS particles (more than 90%) exhibited wurtzite structure, and a small amount were identified as sphalerite-type. Only for a negligibly small portion of the octadecylamine-coated nanoparticles (about 1% or less) the TEM analysis provided acceptable evidence for core/shell structure (Figure 1a).

About 2% of the particles analyzed in the TEM could not be identified reliably to distinguish between wurtzite-type CdS or sphalerite-type ZnS. Emission spectroscopy, however, did not provide evidence for the presence of nanocrystals with bandgaps smaller than about 3.2 eV suggesting that CdS was not present. Varying the excitation wavelength from 600 to 380 nm for diluted suspensions and for solid samples did not cause shifts in the emission band and did not result in new emission peaks characteristic of QDs of cadmium chalcogenides, such as CdS or Cd_2SeS (Figure 2a,b). This finding indicates that most probably the crystalline nanoparticles, for which we could not be identified unambiguously in the TEM, were composed of broadband zinc chalcogenides.

For exchanging the ODA with pyridine ligands we used a coagulation-and-resuspension procedure. About 0.5 mL of 2 mg mL^{-1} of nanoparticles were precipitated with ethanol, centrifuged at 9000 rpm for 10 min and the clear liquid decanted. Pyridine (0.2 mL) was added to the solid pellet, and the particles were resuspended by mild sonication for about 10 min. Hexane was added to precipitate the nanoparticles from the suspension, the liquid decanted after centrifugation, and the solid resuspended in fresh pyridine. The procedure was then repeated two additional times to obtain pyridine-coated nanoparticles, QD-Py, and ligand exchange was confirmed with FTIR. None of the pyridine-coated nanoparticles exhibited core/shell structure (Figure 1b).

For the preparation of the QD-Py/graphene hybrid films, diluted QD-Py suspension was dropped on graphene surfaces. After 1 min, the samples were rinsed with copious amounts of ethanol several times. This process was repeated three to five times. The stacked structures for the TA studies were assembled by placing cover glass slips (each coated with QD-Py/graphene films on one side) on top of one other, separated with ≈100-μm spacer positioned at the slip edges, fixed together with transparent tape. Thus, the QD-Py/graphene films were not in contact with the films or the bare glass surfaces on the neighboring slips.

For the FET devices, the CVD-fabricated graphene was deposited on Si, coated with 300-μm SiO_2. The graphene layer was patterned into rectangles using photolithography and oxygen plasma as implemented by reactive ion etching. The drain and the source terminals were patterned at the edges of the graphene rectangles (at 70 μm separation) via vapor deposition of 2-nm Ti (for improved adhesion of the electrode) and 80-nm gold. Similarly, coating the back of the device with 2-nm Ti and 100-nm gold formed the gate terminal (Scheme 2).

Electron Microscopy: The scanning electron microscopy (SEM) images were recorded with Leo SUPRA 55 microscope. Transmission electron microscopy (TEM) was performed with a FEI-Philips CM300 microscope, operating at 200 and 300 kV accelerating voltage, equipped with a LaB_6 electron gun, an EDAX energy-dispersive spectrometer (EDS) and Gatan MSC794 digital camera. Samples were prepared by dispersing the powder nanoparticles in distilled water through ultrasonic agitation and depositing a drop of the resulting suspension onto copper TEM grids coated with a thin amorphous carbon support film. High-resolution images were obtained by recording through-focus series of images close to Scherzer defocus for individual particles and particle aggregates. Phase identification was based on lattice spacings, measured from fast Fourier transform (FFT) of the HRTEM images of each particle (Figure 1a, b).

Fluorescence Microscopy: The fluorescence images were recorded using a BD Pathway 855 HT confocal microscope, equipped with Olympus objectives (2×, NA = 0.08; and 20×, NA = 0.75; NA = numerical aperture), a xenon arc lamp, a 488 nm (10-nm bandwidth) bandpass excitation filter, a LP dichroic mirror (495 nm cutoff wavelength), a 624 nm (40-nm bandwidth) emission bandpass filter, and a CCD camera. To image large-area samples using the 2× objective, a montage was built from individual images, each consisting of 1024 × 1344 pixels and representing a 3.197 mm × 4.196 mm region (image pixel area = 3.122 μm^2). For higher-resolution imaging, the 20× objective was used and each pixel on the images covered an area of 312 nm^2. To correct for uneven illumination throughout the wide fields of view, each recorded image, $I(x,y)$, was divided by a background image, $I_{BG}(x,y)$, that is, an image of a uniformly fluorescent sample collected using the same optical path, normalized for the average background intensity, $\langle I_{BG} \rangle$: i.e., $I_{corrected}(x,y) = \langle I_{BG} \rangle I(x,y)/I_{BG}(x,y)$.

Cyclic Voltammetry: The cyclic voltammetry (CV) measurements were conducted at ambient room temperature using a Reference 600 potentiostat-galvanostat (Gamry Instruments, Warminster, PA), equipped with a three-electrode cell. A glassy carbon electrode was employed as a working electrode. A Pt wire and saturated calomel electrode (Gamry Instruments) ware used for a counter electrode and a reference electrode, respectively. Before and after the measurements, the reference electrodes were stored in saturated solution of KCl. To prevent contamination, the reference electrode was brought into contact with the sample solutions via a salt bridge. The samples of nanoparticles were suspended in anhydrous acetonitrile electrolyte solutions containing 0.1 M tetrabutylammonium hexafluorophosphate. Prior to each scan, the electrolyte suspension of nanoparticles was purged with pure argon gas, and the voltammograms were recorded at scan rate of 50 mV s^{-1}. After completing the CV measurements for each sample, ferrocene was added to the solution and its half potential was compared with the previously reported value, 0.45 V vs SCE (SCE = saturated calomel electrode).[42] For the QD-ODA samples, we observed (Supporting Information Figure S3): (1) a reversible wave with $E^{(1/2)} = -0.82$ V vs SCE; (2) an irreversible wave with an anodic peak, $E_A = -1.6$ V vs SCE; and (2) an irreversible wave with a cathodic peak, $E_C = 1.2$ V vs SCE. For the QD-Py, we observed similar voltammograms with: (1) a reversible reduction wave with $E^{(1/2)} = -0.86$ V vs SCE; (2) an irreversible reduction wave with $E_A = -1.9$ V vs. SCE; and (3) two irreversible oxidation waves with cathodic peak potentials at 1.2 and 1.9 V vs SCE. After several oxidation scans of the pyridine-coated QDs, an additional anodic peak at –0.6 V vs SCE appeared. Considering that the SCE potential (multiplied by the Faraday constant) is 4.68 eV under the energy of an electron at rest in vacuum,[43] and using the data for the reversible reduction waves, we estimated that the lowest energy levels of the conduction band (or of the lowest unoccupied molecular orbitals, LUMOs) of the QD-ODA and QD-Py were at –3.86 eV and –3.82 eV vs the vacuum level.

Absorption and Emission Spectroscopy: Steady-state UV/visible absorption spectra were recorded using a JASCO V-670 spectrophotometer (Tokyo, Japan). For the liquid samples, we used the double-beam instrument in a transmission mode. For the solid film samples, e.g., QDs film on glass slides and QD/graphene hybrid solid samples, the absorption spectra were obtained from diffuse reflectance spectroscopy measurements using a 60 mm ψ integrating sphere equipped with an individual detector (Model ISN-723, JASCO, Japan). For baseline, a transparent glass slide as a blank was used, and under identical settings the reflection spectra of the solid samples were recorded with the film, coating the sides, facing the integrating sphere. For all samples of solid films and for the glass blank, aluminum foil as a back-reflector was placed behind the glass slides. The absorption spectrum, A vs. λ, was determined from the reflectance, R: $A(\lambda) = -(1/2)\ \lg(R(\lambda))$, where the division by 2 accounted for the reflector on the back of the transparent substrates.

Steady-state emission measurements were conducted using a FluoroLog-3 spectrofluorometer (Horiba-Jobin-Yvon) equipped with double-grating monochromators and a TBX single-photon-counting detector. For the liquid samples, we used right-angle settings, and for the solid-film samples, the emission was recorded at small-angle configuration.[44]

The fluorescence quantum yields, Φ_f, of the liquid sample were estimated from absorbance measured in transmission mode, and emission measured at right-angle settings, at room temperature using 10 mm optical-length quartz cuvette. For reference, we used a solution of rhodamine 6G in ethanol ($\Phi_{f0} = 0.94$). All solution samples were purged with N_2. For the solid films, i.e., QDs on glass slides and the QD/graphene hybrid solid samples, the quantum yields were calculated from small-angle emission measurements and from the reflectance at the excitation wavelength ($\lambda_{ex} = 600$ nm). For the solid glass-slide samples, a solution of the reference was placed in a 2 mm optical-length quartz cuvette, and mounted on the sample holder of the integrating sphere and on the small-angle emission setup.

Time-resolved emission measurements of the solid films were conducted in a reflection mode with a FluoroLog-3 spectrofluorometer (Horiba-Jobin-Yvon) and a NanoLED laser was used for an excitation source

(λ_{ex} = 406 nm; half-height pulse width, $W_{1/2}$ = 195 ps). The intensity of the excitation light was attenuated by placing reflection neutral-density filters on the beam path. For recording the profile of the excitation pulse (i.e., the instrument response function), we used aqueous solution of bovine serum albumin as a scatterer, setting $\lambda_{em} = \lambda_{ex} = 406$ nm. The fluorescence decays were collected near the QD emission maxima, λ_{em} = 630 nm, and fitted to mono- and multi-exponential functions via a deconvolution algorithm. The quality of the fits was monitored by examination of the residuals. All least-squares data fits were conducted using Igor Pro, version 6 (Wavematrics, Inc.) on MacOS and Windows XP workstations. There is a key limitation in the use of emission spectroscopy for characterizing strongly quenched heterogeneous systems such as QD-Py/graphene hybrid films. For luminophores with emission quantum yields smaller than 0.01, however, ensemble-average measurements represent less than 1% of the photoinitiated events. Therefore, we resorted to TA study.

Transient Absorption Spectroscopy: The TA spectra were recorded in transmission mode using a Helios pump-probe spectrometer (Ultrafast Systems, LLC, Florida) equipped with a delay stage allowing maximum probe delays of 3.2 ns at 7 fs temporal step resolution, and whit white-light generators providing UV/visible spectral range from 350 to 800 nm.

The laser source for the Helios was a SpitFire Pro 35F regenerative amplifier (Spectra Physics/ Newport) generating 800-nm pulses (38 fs, 3.5 mJ, 55 nm bandwidth) at 1 kHz repetition rate. The amplifier was pumped with an Empower 30 Q-switched laser ran at 20 W, and a MaiTai SP oscillator provided the seed beam.

For the pump, 500 mW of the amplifier output was sent into an optical parametric amplifier, OPA-800CU (Newport), equipped with a second- and forth-harmonic generators, 2G and 4G, respectively. For the reported data, the signal was tuned between 1520 and 1,600 nm and the 4G output (380 to 400 nm) was sent to the Helios spectrometer, passed through an attenuating filter, a depolarizer, a chopper (blocking every other pump pulse), and converged on the sample surface (about 2 mm beam diameter). The pump power was tuned between 1 and 5 μJ per pulse, which allowed for establishing the changes in the TA spectra due to the increase in the electron population in the CdSe conduction band.[26a] The analysis in this manuscript is based on TA data for which the pump was tuned to 400 nm with energy of 1.5 μJ per pulse.

For the probe, 10 mW of the amplifier output were reflected several meters back and forth over the table (to compensate for the pump delay in the OPA), introduced into the Helios, passed through the delay stage, the white-light generator, and focused on the sample surfaces, ensuring complete overlap by the pump beam. To obtain reasonable TA signal-to-noise ratios for the QD-Py/graphene samples, we used stacks of thin glass substrates, i.e., microscope cover slips one-sidedly coated with single-sheet graphene and QDs. Namely, we probed a stack of QD-Py/graphene monolayers separated from one another by hundreds of micrometers of dielectric, and a total optical density exceeding the ground-state absorption of the QD films with no graphene. For the samples of stacked cover slips, the recorded Raman-scattering repose of the blank samples provided the data for the chirp correction as implemented by using Surface Xplorer (Ultrafast Systems, LLC). The transient kinetics was analyzed using Surface Xplorer and Igor Pro. To exclude the spatial mismatching of the pump and probe for stacked cover slips, we aligned the pump and probe to make sure they over lapped at the entering and the exiting of the sample. The diameter of the pump beam is larger than the probe beam's making the overlap possible for the angle, at which the two beams cross each other in the sample.

Photoelectrical Measurements: The current-voltage measurements were carried out at room temperature, using an HP 4156B semiconductor parameter analyzer. For the investigating the photoinduced effects, the graphene films on the FET devices were illuminated with an UV lamp (365 nm) and power density of 0.2 W/cm^2.

Supporting Information

Supporting Information is available from the Wiley Online Library or from the author.

Acknowledgements

Funding for this research was provided by the U. S. National Science Foundation (CBET 0935995 and CMMI 0800680), the Materials Research Science and Engineering Center (NSF-MRSEC) on Polymers (0213695), and the Nanoscale Science and Engineering Center (NSF-NSEC) on hierarchical manufacturing (CHM 0531171), the Winston Chung Global Energy Center at UCR, and the Riverside Public Utilities. The transient-absorption studies were conducted at the Biophotonics Facilities for Ultrafast Dynamics at the University of California, Riverside, established with funding from the U.S. National Science Foundation (CBET 0923408). The electron-microscopy studies were conducted at the Central Facility for Advanced Microscopy and Microanalysis at the University of California, Riverside, established with funding from the U.S. National Science Foundation.

Received: December 10, 2012
Revised: February 26, 2013
Published online: May 6, 2013

[1] a) I. V. Lightcap, P. V. Kamat, *J. Am. Chem. Soc.* **2012**, *134*, 7109; b) Q. Li, B. Guo, J. Yu, J. Ran, B. Zhang, H. Yan, J. R. Gong, *J. Am. Chem. Soc.* **2011**, *133*, 10878; c) P. K. Santra, P. V. Kamat, *J. Am. Chem. Soc.* **2012**, *134*, 2508; d) T. Dufaux, J. Boettcher, M. Burghard, K. Kern, *Small* **2010**, *6*, 1868; e) C. X. Guo, H. B. Yang, Z. M. Sheng, Z. S. Lu, Q. L. Song, C. M. Li, *Angew. Chem., Int. Ed.* **2010**, *49*, 3014.

[2] a) H. Bi, F.-Q. Huang, J. Liang, X.-M. Xie, M.-H. Jiang, *Adv. Mater.* **2011**, *23*, 3202; b) C.-L. Hsu, C.-T. Lin, J.-H. Huang, C.-W. Chu, K.-H. Wei, L.-J. Li, *ACS Nano* **2012**, *6*, 5031; c) X. Geng, L. Niu, Z. Xing, R. Song, G. Liu, M. Sun, G. Cheng, H. Zhong, Z. Liu, Z. Zhang, L. Sun, H. Xu, L. Lu, L. Liu, *Adv. Mater.* **2010**, *22*, 638; d) G. Eda, M. Chhowalla, *Adv. Mater.* **2010**, *22*, 2392.

[3] a) A. Gray, M. Balooch, S. Allegret, S. De Gendt, W.-E. Wang, *J. Appl. Phys.* **2008**, *104*, 053109; b) I. Jung, M. Vaupel, M. Pelton, R. Piner, D. A. Dikin, S. Stankovich, J. An, R. S. Ruoff, *J. Phys. Chem. C* **2008**, *112*, 8499; c) C. Lee, J. Y. Kim, S. Bae, K. S. Kim, B. H. Hong, E. J. Choi, *Appl. Phys. Lett.* **2011**, *98*, 071905.

[4] a) B. Gao, G. Hartland, T. Fang, M. Kelly, D. Jena, H. Xing, L. Huang, *Nano Lett.* **2011**, *11*, 3184; b) L. Huang, B. Gao, G. Hartland, M. Kelly, H. Xing, *Surf. Sci.* **2011**, *605*, 1657.

[5] a) A. P. Alivisatos, I. Gur, N. A. Fromer, C. P. Chen, A. G. Kanaras, *Nano Lett.* **2007**, *7*, 409; b) X. G. Peng, *Acc. Chem. Res.* **2010**, *43*, 1387.

[6] R. Loef, A. J. Houtepen, E. Talgorn, J. Schoonman, A. Goossens, *Nano Lett.* **2009**, *9*, 856.

[7] a) P. V. Kamat, *J. Phys. Chem. C* **2008**, *112*, 18737; b) P. V. Kamat, *Acc. Chem. Res.* **2012**, *45*, 1906.

[8] a) O. K. Farha, C. E. Wilmer, I. Eryazici, B. G. Hauser, P. A. Parilla, K. O'Neill, A. A. Sarjeant, S. T. Nguyen, R. Q. Snurr, J. T. Hupp, *J. Am. Chem. Soc.* **2012**, *134*, 9860; b) H.-J. Son, X. Wang, C. Prasittichai, N. C. Jeong, T. Aaltonen, R. G. Gordon, J. T. Hupp, *J. Am. Chem. Soc.* **2012**, *134*, 9537; c) P. Diao, Z. Liu, *Adv. Mater.* **2010**, *22*, 1430; d) N. R. de Tacconi, W. Chanmanee, K. Rajeshwar, J. Rochford, E. Galoppini, *J. Phys. Chem. C* **2009**, *113*, 2996; e) A. Kongkanand, K. Tvrdy, K. Takechi, M. Kuno, P. V. Kamat, *J. Am. Chem. Soc.* **2008**, *130*, 4007; f) T. Hasobe, S. Fukuzumi, P. V. Kamat, *Angew. Chem., Int. Ed.* **2006**, *45*, 755.

[9] a) S. Chaudhary, H. Lu, A. M. Mueller, C. J. Bardeen, M. Ozkan, *Nano Lett.* **2007**, *7*, 1973; b) S. Ren, M. Bernardi, R. R. Lunt, V. Bulovic, J. C. Grossman, S. Gradecak, *Nano Lett.* **2011**, *11*, 5316; c) Q. Wang, K. Zhu, N. R. Neale, A. J. Frank, *Nano Lett.* **2009**, *9*, 806; d) G. M. A. Rahman, D. M. Guldi, R. Cagnoli, A. Mucci, L. Schenetti, L. Vaccari, M. Prato, *J. Am. Chem. Soc.* **2005**, *127*, 10051.

[10] K. S. Novoselov, A. K. Geim, S. V. Morozov, D. Jiang, Y. Zhang, S. V. Dubonos, I. V. Grigorieva, A. A. Firsov, *Science* **2004**, *306*, 666.
[11] a) F. Bonaccorso, Z. Sun, T. Hasan, A. C. Ferrari, *Nat. Photonics* **2010**, *4*, 611; b) X. Wan, Y. Huang, Y. Chen, *Acc. Chem. Res.* **2012**, *45*, 598.
[12] a) A. N. Cao, Z. Liu, S. S. Chu, M. H. Wu, Z. M. Ye, Z. W. Cai, Y. L. Chang, S. F. Wang, Q. H. Gong, Y. F. Liu, *Adv. Mater.* **2010**, *22*, 103; b) K. P. Loh, Q. L. Bao, G. Eda, M. Chhowalla, *Nat. Chem.* **2010**, *2*, 1015.
[13] a) M. J. Allen, J. D. Fowler, V. C. Tung, Y. Yang, B. H. Weiller, R. B. Kaner, *Appl. Phys. Lett.* **2008**, *93*, 193119; b) L. J. Cote, R. Cruz-Silva, J. X. Huang, *J. Am. Chem. Soc.* **2009**, *131*, 11027; c) H. Yamaguchi, G. Eda, C. Mattevi, H. Kim, M. Chhowalla, *ACS Nano* **2010**, *4*, 524.
[14] a) S. Bae, H. Kim, Y. Lee, X. F. Xu, J. S. Park, Y. Zheng, J. Balakrishnan, T. Lei, H. R. Kim, Y. I. Song, Y. J. Kim, K. S. Kim, B. Ozyilmaz, J. H. Ahn, B. H. Hong, S. Iijima, *Nat. Nanotechnol.* **2010**, *5*, 574; b) X. Li, W. Cai, J. An, S. Kim, J. Nah, D. Yang, R. Piner, A. Velamakanni, I. Jung, E. Tutuc, S. K. Banerjee, L. Colombo, R. S. Ruoff, *Science* **2009**, *324*, 1312; c) D. A. C. Brownson, R. V. Gorbachev, S. J. Haigh, C. E. Banks, *Analyst* **2012**, *137*, 833; d) S. Guo, M. Ghazinejad, X. Qin, H. Sun, W. Wang, F. Zaera, M. Ozkan, C. S. Ozkan, *Small* **2012**, *8*, 1073; e) J. R. Kyle, A. Guvenc, W. Wang, M. Ghazinejad, J. Lin, S. Guo, C. S. Ozkan, M. Ozkan, *Small* **2011**, *7*, 2599.
[15] K. S. Kim, Y. Zhao, H. Jang, S. Y. Lee, J. M. Kim, K. S. Kim, J.-H. Ahn, P. Kim, J.-Y. Choi, B. H. Hong, *Nature* **2009**, *457*, 706.
[16] a) Z. Y. Chen, S. Berciaud, C. Nuckolls, T. F. Heinz, L. E. Brus, *ACS Nano* **2010**, *4*, 2964; b) A. V. Klekachev, M. Cantoro, M. H. van der Veen, A. L. Stesmans, M. M. Heyns, S. De Gendt, *Physica E* **2011**, *43*, 1046.
[17] T. Förster, *Ann. Phys.* **1948**, *2*, 55.
[18] D. L. Dexter, *J. Chem. Phys.* **1953**, *21*, 836.
[19] a) H. Lu, D. Bao, M. Penchev, M. Ghazinejad, V. I. Vullev, C. S. Ozkan, M. Ozkan, *Adv. Sci. Lett.* **2010**, *3*, 101; b) B. Xia, D. Bao, S. Upadhyayula, G. Jones II, V. I. Vullev, *J. Org. Chem.* **2013**, *78*, 1994.
[20] S. Jeong, H. C. Shim, S. Kim, C. S. Han, *ACS Nano* **2010**, *4*, 324.
[21] X. M. Geng, L. Niu, Z. Y. Xing, R. S. Song, G. T. Liu, M. T. Sun, G. S. Cheng, H. J. Zhong, Z. H. Liu, Z. J. Zhang, L. F. Sun, H. X. Xu, L. Lu, L. W. Liu, *Adv. Mater.* **2010**, *22*, 638.
[22] a) Q. W. Li, B. Q. Sun, I. A. Kinloch, D. Zhi, H. Sirringhaus, A. H. Windle, *Chem. Mater.* **2006**, *18*, 164; b) B. H. Juarez, M. Meyns, A. Chanaewa, Y. X. Cai, C. Klinke, H. Weller, *J. Am. Chem. Soc.* **2008**, *130*, 15282; c) C. G. Lu, A. Akey, W. Wang, I. P. Herman, *J. Am. Chem. Soc.* **2009**, *131*, 3446.
[23] a) A. C. Carter, C. E. Bouldin, K. M. Kemner, M. I. Bell, J. C. Woicik, S. A. Majetich, *Phys. Rev. B* **1997**, *55*, 13822; b) M. G. Berrettini, G. Braun, J. G. Hu, G. F. Strouse, *J. Am. Chem. Soc.* **2004**, *126*, 7063.
[24] a) M. Egli, V. Tereshko, G. N. Mushudov, R. Sanishvili, X. Y. Liu, F. D. Lewis, *J. Am. Chem. Soc.* **2003**, *125*, 10842; b) R. Meurisse, R. Brasseur, A. Thomas, *Biochim. Biophys. Acta* **2003**, *1649*, 85; c) I. Ohno, M. Tomizawa, N. Miyazu, G. Kushibiki, K. Noda, Y. Hasebe, K. A. Durkin, T. Miyake, S. Kagabu, *Bioorg. Med. Chem. Lett.* **2010**, *20*, 5933.
[25] J. Wan, A. Ferreira, W. Xia, C. H. Chow, K. Takechi, P. V. Kamat, G. Jones, V. I. Vullev, *J. Photochem. Photobiol., A* **2008**, *197*, 364.
[26] a) V. I. Klimov, *J. Phys. Chem. B* **2000**, *104*, 6112; b) A. J. Morris-Cohen, M. T. Frederick, L. C. Cass, E. A. Weiss, *J. Am. Chem. Soc.* **2011**, *133*, 10146; c) C. Burda, S. Link, M. Mohamed, M. El-Sayed, *J. Phys. Chem. B* **2001**, *105*, 12286.
[27] D. J. Norris, A. Sacra, C. B. Murray, M. G. Bawendi, *Phys. Rev. Lett.* **1994**, *72*, 2612.
[28] A. I. Ekimov, F. Hache, M. C. Schanneklein, D. Ricard, C. Flytzanis, I. A. Kudryavtsev, T. V. Yazeva, A. V. Rodina, A. L. Efros, *J. Opt. Soc. Am. B* **1993**, *10*, 100.
[29] V. I. Klimov, A. A. Mikhailovsky, D. W. McBranch, C. A. Leatherdale, M. G. Bawendi, *Phys. Rev. B* **2000**, *61*, 13349.
[30] a) V. Chikan, D. F. Kelley, *Nano Lett.* **2002**, *2*, 1015; b) P. Guyot-Sionnest, M. Shim, C. Matranga, M. Hines, *Phys. Rev. B* **1999**, *60*, R2181.
[31] a) K. Enomoto, J. A. LaVerne, S. Seki, S. Tagawa, *J. Phys. Chem. A* **2006**, *110*, 9874; b) G. R. Dey, D. B. Naik, P. Dwibedy, K. Kishore, *Radiat. Phys. Chem.* **2002**, *64*, 395.
[32] B. Farrow, P. V. Kamat, *J. Am. Chem. Soc.* **2009**, *131*, 11124.
[33] A. Pandey, P. Guyot-Sionnest, *J. Phys. Chem. Lett.* **2010**, *1*, 45.
[34] C. Burda, T. C. Green, S. Link, M. A. El-Sayed, *J. Phys. Chem. B* **1999**, *103*, 1783.
[35] a) G. X. Ni, Y. Zheng, S. Bae, H. R. Kim, A. Pachoud, Y. S. Kim, C. L. Tan, D. Im, J. H. Ahn, B. H. Hong, B. Ozyilmaz, *ACS Nano* **2012**, *6*, 1158; b) J. Lee, L. Tao, Y. Hao, R. S. Ruoff, D. Akinwande, *Appl. Phys. Lett.* **2012**, *100*.
[36] J. H. Chen, C. Jang, S. Adam, M. S. Fuhrer, E. D. Williams, M. Ishigami, *Nat. Phys.* **2008**, *4*, 377.
[37] a) J. Lin, D. Teweldebrhan, K. Ashraf, G. Liu, X. Jing, Z. Yan, R. Li, M. Ozkan, R. K. Lake, A. A. Balandin, C. S. Ozkan, *Small* **2010**, *6*, 1150; b) P. K. Ang, M. Jaiswal, C. H. Y. X. Lim, Y. Wang, J. Sankaran, A. Li, C. T. Lim, T. Wohland, O. Barbaros, K. P. Loh, *ACS Nano* **2010**, *4*, 7387.
[38] a) J. G. Radich, P. V. Kamat, *ACS Catal.* **2012**, *2*, 807; b) R. K. Paul, M. Ghazinejad, M. Penchev, J. Lin, M. Ozkan, C. S. Ozkan, *Small* **2010**, *6*, 2309; c) J. Lin, J. Zhong, D. Bao, J. Reiber-Kyle, W. Wang, V. Vullev, M. Ozkan, C. S. Ozkan, *J. Nanosci. Nanotechnol.* **2012**, *12*, 1770; d) W. Wang, S. Guo, M. Penchev, J. Zhong, J. Lin, D. Bao, V. Vullev, M. Ozkan, C. S. Ozkan, *J. Nanosci. Nanotechnol.* **2012**, *12*, 6913.
[39] a) J. O. Hwang, J. S. Park, D. S. Choi, J. Y. Kim, S. H. Lee, K. E. Lee, Y.-H. Kim, M. H. Song, S. Yoo, S. O. Kim, *ACS Nano* **2012**, *6*, 159; b) A. Misra, M. Waikar, A. Gour, H. Kalita, M. Khare, M. Aslam, A. Kottantharayil, *Appl. Phys. Lett.* **2012**, *100*, 233506; c) Y.-J. Yu, Y. Zhao, S. Ryu, L. E. Brus, K. S. Kim, P. Kim, *Nano Lett.* **2009**, *9*, 3430.
[40] A. H. Castro Neto, F. Guinea, N. M. R. Peres, K. S. Novoselov, A. K. Geim, *Rev. Mod. Phys.* **2009**, *81*, 109.
[41] a) V. Huynh My Hang, J. Meyer Thomas, *Chem. Rev.* **2007**, *107*, 5004; b) J. M. Mayer, *Annu. Rev. Phys. Chem.* **2004**, *55*, 363; c) R. I. Cukier, D. G. Nocera, *Annu. Rev. Phys. Chem.* **1998**, *49*, 337.
[42] D. Bao, B. Millare, W. Xia, B. G. Steyer, A. A. Gerasimenko, A. Ferreira, A. Contreras, V. I. Vullev, *J. Phys. Chem. A* **2009**, *113*, 1259.
[43] S. Trasatti, *Pure Appl. Chem.* **1986**, *58*, 955.
[44] J. Wan, M. S. Thomas, S. Guthrie, V. I. Vullev, *Ann. Biomed. Eng.* **2009**, *37*, 1190.